




Reconfigurable spin tunneling diode and giant tunneling magnetoresistance in a symmetric van der Waals double-barrier magnetic tunnel junction

Y. Zhu ^{1,2} X. Y. Guo,¹ B. Y. Chi,^{2,3} Y. Yan ^{1,*} and X. F. Han ^{2,3,4,†}

¹Key Laboratory of Physics and Technology for Advanced Batteries (Ministry of Education), Department of Physics, Jilin University, Changchun 130012, China

²Center of Materials Science and Optoelectronics Engineering, University of Chinese Academy of Sciences, Beijing 100049, China

³Beijing National Laboratory for Condensed Matter Physics, Institute of Physics, University of Chinese Academy of Sciences, Chinese Academy of Sciences, Beijing 100190, China

⁴Songshan Lake Materials Laboratory, Dongguan, Guangdong 523808, China



(Received 24 January 2024; revised 3 July 2024; accepted 22 July 2024; published 5 August 2024)

The tunneling diodes are commonly used to control the direction of current in semiconductor devices and are an essential circuit element in modern electronics. Here, we propose a multifunctional and reconfigurable spin-dependent tunneling diode (spin TD) based on a symmetric van der Waals (vdW) double-barrier magnetic tunnel junction (DBMTJ), where if the magnetic moments of two ferromagnetic electrodes are antiparallel, a significant spin TD effect is produced in the symmetric vdW DBMTJ due to the spin splitting of the middle ferromagnetic metal layer. Using first-principles calculations, we find that the proposed spin TD effect and three significantly different resistance states with giant tunneling magnetoresistance are achieved in the vdW DBMTJs based on the $\text{Fe}_3\text{GaTe}_2/\text{GeI}_2/\text{Fe}_3\text{GaTe}_2/\text{GeI}_2/\text{Fe}_3\text{GaTe}_2$ and $\text{Fe}_3\text{GaTe}_2/\text{GeI}_2/\text{Fe}_3\text{GeTe}_2/\text{GeI}_2/\text{Fe}_3\text{GaTe}_2$ vdW heterostructures. Moreover, the spin TD effect can be modulated by changing the magnetic configuration of the symmetric vdW DBMTJ through the magnetic field. Our work holds valuable implications for developing multifunctional and reconfigurable nondoped diode devices.

DOI: [10.1103/PhysRevB.110.054409](https://doi.org/10.1103/PhysRevB.110.054409)

I. INTRODUCTION

As a crucial electronic component, the diode has served various circuits, including rectification, protection, switching, signal conditioning, and so on [1–7]. Recently, conventional diode devices have encountered challenges in rapidly processing extensive volumes of data information and miniaturizing devices. Typically, P-N junction diodes exhibit varying space charge regions under bias, leading to different conduction states [8]. Correspondingly, the application of P-N junction diodes in high-frequency devices is constrained by slow charge redistribution during state switching. Moreover, the interface defects significantly affect performance and reliability of P-N junction diodes based on bulk materials in the case of miniaturization of diodes [9].

In recent years, van der Waals (vdW) magnetic tunneling diodes with vdW magnetic electrodes provide a new opportunity for designing innovative multifunctional diodes [10–12]. As known, the vdW materials without dangling bonds on the surface hold promise for the creation of high-quality and high-performance microjunction devices, and the inherently rapid electron tunneling process in vdW tunnel junctions makes them well-suited for use in high-frequency devices [13–16]. More importantly, the tunneling magnetoresistance (TMR) effect and nonvolatile programming of the controllable

current-voltage characteristics in vdW magnetic tunneling diodes can allow the combination of nonvolatility, reconfigurability, and multifunctionality on the diode. Recently vdW magnetic tunnel junctions based on a semimetallic magnet (SMM)/spin-gapless semiconductor (SGS) heterostructure are reported to produce a spin tunneling diode effect [17–19]. However, the relatively small TMR value and less resistance states constrain their applicability in memory devices and logic circuits. Meanwhile, the choice of materials for this vdW magnetic tunnel diode becomes a more intricate task due to specialized band structures of vdW SMMs and SGSs. In addition, the prevailing approach in diode device fabrication involves carrier doping of distinct types [20,21]. Therefore, in order to address these challenges faced by diodes and make device manufacturing easier, there is a compelling need to design innovative multifunctional vdW nondoped diode devices.

It is known that the majority-spin and minority-spin energy levels of the middle ferromagnetic (FM) metal layer in a symmetric double-barrier magnetic tunnel junction (DBMTJ) based on FM electrode/nonmagnetic insulator/FM metal/nonmagnetic insulator/FM electrode (FME/NMI/FMM/NMI/FME) vdW heterostructure are spin splitting [22]. When the magnetic moments of the FMEs are antiparallel, the spin splitting of the middle FMM layer of the DBMTJ can lead to a substantial disparity between the majority-spin (minority-spin) current under positive bias, +V, and that under negative bias, -V, ultimately yielding a pronounced diode effect within the DBMTJ device.

*Contact author: yanyu@jlu.edu.cn

†Contact author: xfhan@iphy.ac.cn

In this work, we propose a multifunctional and reconfigurable spin tunneling diode (spin TD) based on symmetric vdW DBMTJ and calculate the spin-resolved transport characteristics of the two symmetric vdW DBMTJs based on $\text{Fe}_3\text{GaTe}_2/\text{GeI}_2/\text{Fe}_3\text{GaTe}_2/\text{GeI}_2/\text{Fe}_3\text{GaTe}_2$ and $\text{Fe}_3\text{GaTe}_2/\text{GeI}_2/\text{Fe}_3\text{GeTe}_2/\text{GeI}_2/\text{Fe}_3\text{GaTe}_2$ vdW heterostructures using first-principles calculations, denoted as vdW DBMTJ1 and vdW DBMTJ2. The results reveal vdW DBMTJ1 and vdW DBMTJ2 with three distinct resistive states can achieve giant TMR of $3.61 \times 10^9\%$ and $1.02 \times 10^6\%$, respectively, and in the case of antiparallel states of magnetization of the two FMEs, resonance tunneling occurred at a positive and negative bias, resulting in a significant spin TD effect in the proposed symmetric vdW DBMTJs. Therefore, the proposed vdW DBMTJ not only can achieved giant TMR values and multiresistance states but also can produce a positive spin-resolved conduction and negative cutoff spin diode effect and the spin TD effect can be modulated by changing the magnetic configuration of the vdW DBMTJ through the magnetic field. This means that the proposed symmetric vdW DBMTJ is a multifunctional and reconfigurable nondoped diode.

II. COMPUTATIONAL METHOD

The structure optimization and electronic structure calculations are performed by the Vienna *ab initio* simulation package (VASP) [23,24]. Given that the local spin density approximation (LSDA) provides a more accurate description of the magnetic moment and magnetocrystalline anisotropy properties of Fe_3GaTe_2 compared to the Perdew-Burke-Ernzerhof functional of the generalized gradient approximation, our work employs the LSDA for the exchange-correlation potential [25–28]. The vdW interactions of two-dimensional (2D) materials are treated with the DFT-D3 exchange functional [29]. A plane-wave energy cutoff of 500 eV and a $13 \times 13 \times 1$ Monkhorst-Pack k -point grid are used for the structure optimization and electronic structure calculations. All atomic positions are relaxed until the energy and force are smaller than 1×10^{-5} eV and 0.01 eV/Å, respectively. A vacuum space of 15 Å is used to avoid the interaction between adjacent layers.

The electronic transport calculations are performed using the NANODCAL package based on the nonequilibrium Green's function combined with the density functional theory (DFT) [30,31]. The spin-resolved conductance G_σ of the vdW DBMTJ is calculated using the Landauer-Büttiker formula:

$$G_\sigma = \frac{e^2}{h} \sum_{k_\parallel} T_\sigma(k_\parallel, E_F), \quad (1)$$

where $T_\sigma(k_\parallel, E_F)$ is the transmission coefficient with spin ($\sigma = \uparrow$ and \downarrow) at the Fermi level E_F and the transverse Bloch wave vector k_\parallel ($k_\parallel = k_x, k_y$) perpendicular to the transport direction. Here, e and h are the electron charge and the Planck constant, respectively.

At bias voltage V , the spin-resolved current is calculated as follows:

$$I_\sigma = \frac{e}{h} \int_{\mu_2}^{\mu_1} T_\sigma(E, V) [f_1(E) - f_2(E)] dE, \quad (2)$$

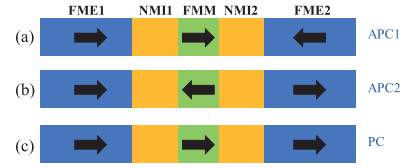


FIG. 1. Schematic diagram of structure of the vdW DBMTJ for the (a) APC1, (b) APC2, and (c) PC magnetic configurations. Navy blue, green, and yellow rectangles represent FM electrodes (FMEs), FM metal (FMM) layers, and nonmagnetic insulator (NMI) barriers, respectively. Black arrow indicates the direction of magnetic moment.

where $T_\sigma(E, V)$ is the transmission coefficient with spin σ at energy E under the applied bias voltage V , $f_1(E)$ [$f_2(E)$] is the Fermi distribution function of electrons in electrode 1 (electrode 2), and μ_1 (μ_2) is the electrochemical potential of electrode 1 (electrode 2).

The cutoff energy of 80 hartree and the double- ζ atomic orbital basis are used for the transport calculations. A $11 \times 11 \times 1$ k mesh is used for self-consistent calculations. The k points for the spin-resolved transmission coefficient and current calculations are $150 \times 150 \times 1$, which is tested.

III. RESULTS AND DISCUSSIONS

In the symmetric vdW DBMTJ based on the FME/NMI/FMM/NMI/FME heterostructure, there are three magnetic configurations. When the magnetizations of the two FMEs are antiparallel, the magnetic moment of the middle FMM layer is parallel to the magnetization of another FME and antiparallel to the magnetization of another FME, resulting in the APC1 state, as shown in Fig. 1(a). When the magnetizations of the two FMEs are parallel, the magnetic moment of the middle FMM layer can be either antiparallel [Fig. 1(b)] or parallel [Fig. 1(c)] to the magnetization of two FMEs, denoted as the APC2 and PC states, respectively.

For the APC1 state of the symmetric vdW DBMTJ, the magnetic moments of two FMEs are antiparallel, the majority-spin transmission (T_\uparrow) is the transmission of electrons from the majority-spin state (red region) of FME1 through the majority-spin state (red region) of the middle FMM layer to the minority-spin state (blue region) of FME2, as shown in Fig. 2(a). Moreover, the minority-spin transmission (T_\downarrow) of the APC1 state corresponds to the transmission of electrons from the minority-spin state (blue region) of FME1 through the minority-spin state (blue region) of the middle FMM layer to the majority-spin state (red region) of FME2. When a bias $\pm V$ is applied to the vdW DBMTJ, the Fermi levels and spin states of the FME1 and FME2 move by $\mp eV/2$ and $\pm eV/2$ relative to those of the FME1 and FME2 at zero bias, respectively, as shown in Figs. 2(c) and 2(e). Due to the spin splitting of the middle FMM layer of the vdW DBMTJ, the T_\uparrow (T_\downarrow) at a positive bias $+V$ is different from T_\downarrow (T_\uparrow) at a negative bias $-V$ for the APC1 state of the vdW DBMTJ. Therefore, the difference between the majority-spin state and the minority-spin state of the FMM layer can lead to a substantial disparity between the transmission spin current of the vdW DBMTJ at

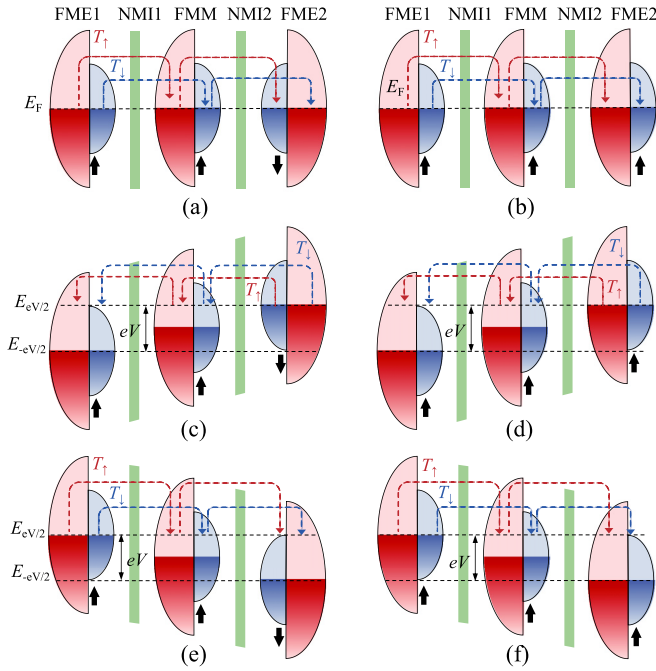


FIG. 2. Schematic diagram of the electronic structure for the APC1 state of vdW DBMTJ at bias voltages of (a) 0 V, (c) +V, and (e) -V. Schematic diagram of the electronic structure for the PC state of the vdW DBMTJ at bias voltages of (b) 0 V, (d) +V, and (f) -V. Red and blue shadows represent the majority-spin state and the minority-spin state, respectively. The black arrows represent the directions of the magnetic moments of FME and FMM. Red and blue dashed lines represent majority-spin transmission (T_{\uparrow}) and the minority-spin transmission (T_{\downarrow}), respectively. Black dashed lines in panels (c)–(f) represent bias windows.

a positive bias +V and that at a negative bias -V, ultimately yielding a spin diode effect for the APC1 state. For the PC state of the vdW DBMTJ, the magnetic moments of two FMEs are parallel, the T_{\uparrow} (T_{\downarrow}) is the transmission of electrons from the majority-spin (minority-spin) state of FME1 through the majority-spin (minority-spin) state of the middle FMM layer to the majority-spin (minority-spin) state of FME2. It can be seen that the distribution for spin states of two FMEs and the middle FMM at a positive bias +V is the same as that at a negative bias -V, as shown in Figs. 2(d) and 2(f), and thus the transmission current of the vdW DBMTJ at a positive bias +V is nearly the same as that at a negative bias -V. Consequently, the diode effect is not produced for the PC state of the symmetric vdW DBMTJ. Similarly, the diode effect can not be produced for the APC2 state of the symmetric vdW DBMTH since the distribution for spin states of two FMEs and the middle FMM layer at a positive bias +V is nearly the same as that at a negative bias -V for the APC2 state. As a result, the spin TD effect can be modulated by changing the magnetic configuration of the vdW DBMTJ through the magnetic field.

In order to prove the proposed spin diode effect in the symmetric vdW DBMTJ, we constructed vdW DBMTJ1 and vdW DBMTJ2 and calculated their spin-resolved transport using first-principles calculations. Fe_3GaTe_2 and Fe_3GeTe_2

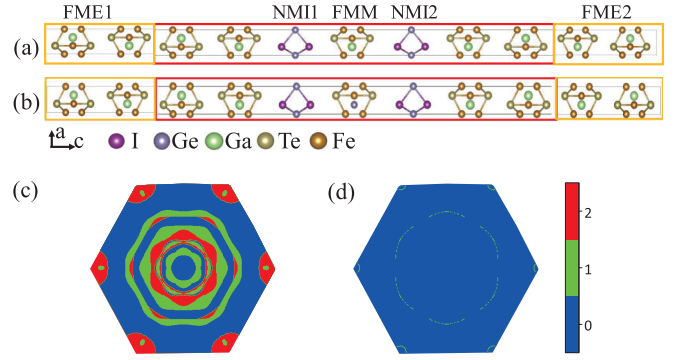


FIG. 3. Side view of the atomic structure of (a) vdW DBMTJ1 and (b) vdW DBMTJ2. Yellow and red bordered areas represent electrodes and scattering regions, respectively. k -resolved (c) majority-spin and (d) minority-spin conductive channels of the Fe_3GaTe_2 electrode in the 2DBZ at the energy of 0 eV.

have been reported to be vdW FM metals with high Curie temperature and perpendicular magnetic anisotropy, making them suitable as electrodes or inserted FM metal layers for tunnel junctions [32–34]. Bulk GeI_2 is a wide-band-gap vdW semiconductor with a band gap of 2.5 eV and the calculated band gap of monolayer GeI_2 is 2.11 eV [35,36]. Moreover, the optimized lattice constant of monolayer GeI_2 is 4.17 Å, which is well matched with the lattice constants of Fe_3GeTe_2 ($a = b = 4.02$ Å) and Fe_3GaTe_2 ($a = b = 4.03$ Å) in vdW DBMTJ1 and vdW DBMTJ2. The atomic structures of vdW DBMTJ1 and vdW DBMTJ2 are shown in Figs. 3(a) and 3(b), respectively, and the lattice constants for vdW DBMTJ1 and vdW DBMTJ2 are set as those of Fe_3GaTe_2 and Fe_3GeTe_2 , respectively. Here we construct the vdW DBMTJ using the most energetically favorable heterostructure obtained by optimizing the interlayer distance and stacking configurations of the $\text{Fe}_3\text{GaTe}_2/\text{GeI}_2/\text{Fe}_3\text{GaTe}_2/\text{GeI}_2/\text{Fe}_3\text{GaTe}_2$ and $\text{Fe}_3\text{GaTe}_2/\text{GeI}_2/\text{Fe}_3\text{GeTe}_2/\text{GeI}_2/\text{Fe}_3\text{GaTe}_2$ heterostructures. In the main text, we primarily focus on the calculated results for vdW DBMTJ1, while the calculation results for vdW DBMTJ2 are presented in Appendices C and D.

Table I shows the conductance and resistance area (RA) products of the vdW DBMTJ1 for the three magnetic configurations under zero bias. It is evident that the conductance of the PC state is much larger than that of the APC1 and APC2 states and the conductance of the APC2 state also markedly exceeds that of the APC1 state. The TMR values between the different magnetic states of the vdW DBMTJ are calculated using the following formula:

$$\text{TMR1} = \frac{G_{\text{PC}} - G_{\text{APC1}}}{G_{\text{APC1}}} \times 100, \quad (3)$$

$$\text{TMR2} = \frac{G_{\text{PC}} - G_{\text{APC2}}}{G_{\text{APC2}}} \times 100, \quad (4)$$

$$\text{TMR3} = \frac{G_{\text{APC2}} - G_{\text{APC1}}}{G_{\text{APC1}}} \times 100. \quad (5)$$

It is notable that the calculated TMR1, TMR2, and TMR3 are as high as $3.61 \times 10^9\%$, $4.85 \times 10^5\%$, and $7.45 \times 10^5\%$, respectively. Meanwhile, the RA product for the PC state is only $3.27 \times 10^{-1} \Omega \mu\text{m}^2$ due to the large conductance, which

TABLE I. Conductance (e^2/h) and RA product ($\Omega \cdot \mu\text{m}^2$) of the vdW DBMTJ1 for three magnetic configurations under zero bias. G_{total} , G_{\uparrow} , and G_{\downarrow} represent the total, majority-spin, and minority-spin conductances, respectively.

	G_{\uparrow}	G_{\downarrow}	$G_{\text{total}}(G_{\uparrow} + G_{\downarrow})$	RA
APC1	2.97×10^{-10}	1.29×10^{-11}	3.10×10^{-10}	1.19×10^7
APC2	2.31×10^{-6}	1.26×10^{-13}	2.31×10^{-6}	1.59×10^3
PC	1.12×10^{-2}	4.33×10^{-14}	1.12×10^{-2}	3.27×10^{-1}

is much smaller than the typical RA products associated with magnetic tunnel junctions with high TMR values [37]. As known, the electron transmission across the vdW DBMTJ is closely related to the intrinsic conduction channels of the FMEs; thus, the distribution of majority-spin and minority-spin conductive channels in the 2D Brillouin zone (2DBZ) of the Fe_3GaTe_2 electrode are calculated to clarify high TMR values of vdW DBMTJ1. As shown in Figs. 3(c) and 3(d), the conductive channels of majority-spin for Fe_3GaTe_2 electrodes are much larger than those of minority-spin, and the nonzero majority-spin channels have almost no overlap with the nonzero minority-spin channels in the 2DBZ, indicating that the Fe_3GaTe_2 electrode is highly spin polarized [28]. Therefore, the majority-spin conductance across vdW DBMTJ1 is much larger than the minority-spin conductance in the PC and APC2 states and the conductance of the APC1 state is very small. Meanwhile, due to strong spin polarization of the middle Fe_3GaTe_2 layer, the majority-spin conductance of the PC state is significantly larger than the majority-spin conductance of the APC2 state, and thus total conductance of the PC state is significantly larger than that of the APC2 state. Consequently, giant TMR values and multiresistance states are generated in vdW DBMTJ1. Similarly, vdW DBMTJ2 can also achieve giant TMR values and multiresistance states, as displayed in Appendix C.

Subsequently, we calculate the spin-resolved transport properties of vdW DBMTJ1 at bias voltage to assess the relationship between current and bias voltage for three magnetic configurations. Figure 4(a) show the spin-resolved current-voltage (I - V) curve for the APC1 state of the vdW DBMTJ1. As can be seen from Fig. 4(a), when the positive bias voltage increases from 0 to 0.3 V, the majority-spin, minority-spin, and total currents almost remain small constants, respectively. It is noteworthy that when the positive bias voltage is further increased from 0.3 to 0.4 V, the minority-spin current rapidly increases with the increase of the bias voltage and reaches the highest at 0.4 V bias, while the majority-spin current still remains a small constant. Conversely, both the majority-spin and minority-spin currents almost remain small constants with the increase of the negative bias voltage, and the majority-spin (total) current slightly increases with the increases of voltage when the bias voltage is increased from -0.3 to -0.35 V, which is considerably lower than the corresponding minority-spin current under positive bias voltage. Consequently, vdW DBMTJ1 exhibits positive minority-spin conduction and a negative cutoff spin diode effect in the APC1 state. In contrast, the majority-spin, minority-spin, and total currents at positive bias voltage are almost same as those at corresponding negative bias voltage in the APC2 and PC states, as shown in Figs. 4(b) and 4(c), indicating that the

diode effect in vdW DBMTJ1 can be regulated by external magnetic fields. Similarly, the reconfigurable spin TD effect also occurs in vdW DBMTJ2, as shown in Appendix D.

Figure 5 shows the spin resolved transmission spectra of the APC1 state in vdW DBMTJ1 under different biases. It is seen from Fig. 5(b) that at a bias voltage of $+0.4$ V, a sharp and high minority-spin transmission peak appears within the bias window and the transmission peak is located at the energy point of 0.17 eV. However, there are no obvious transmission peaks within the bias window when the bias voltages are $+0.3$ and $+0.5$ V. Meanwhile, there is no high-transmission peak within the bias window when the negative bias voltage is in the range of -0.3 to -0.5 V, as shown in Fig. 5. This sharp and high minority-spin transmission peak within the bias window results in the large current under a bias voltage of $+0.4$ V because the current is calculated by integrating transmission coefficients with respect to energies in the bias

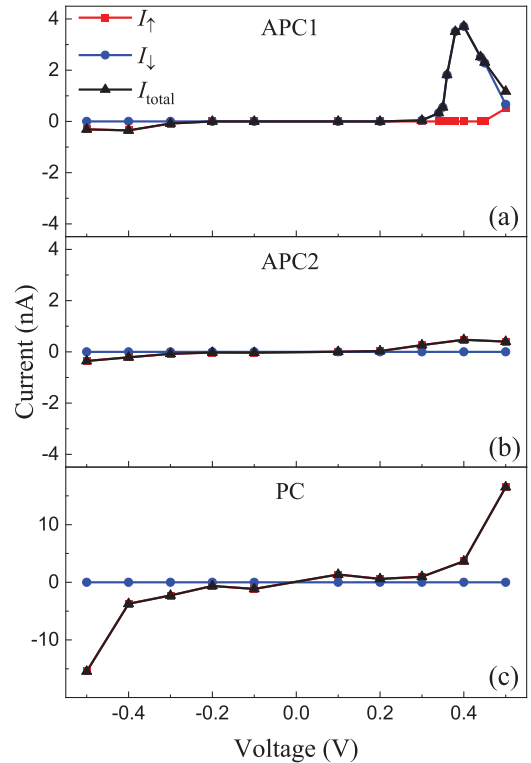


FIG. 4. Spin-resolved current-voltage curve of vdW DBMTJ1 for the (a) APC1, (b) APC2, and (c) PC states. I_{\uparrow} , I_{\downarrow} , and I_{total} ($I_{\uparrow} + I_{\downarrow}$) represent the majority-spin, minority-spin, and total currents, respectively.

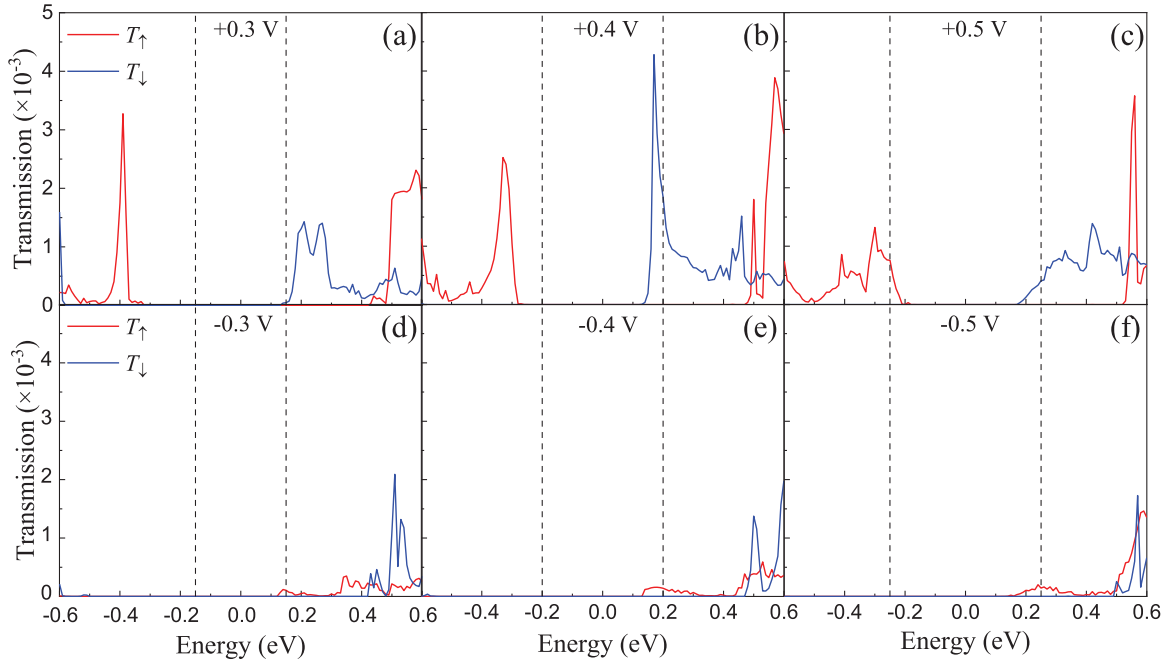


FIG. 5. Spin-resolved transmission spectra of the APC1 state in vdW DBMTJ1 at bias voltages of (a) +0.3 V, (b) +0.4 V, (c) +0.5 V, (d) -0.3 V, (e) -0.4 V, and (f) -0.5 V. The vertical dashed lines represent the bias window. T_{\uparrow} and T_{\downarrow} represent the majority-spin and minority-spin transmissions, respectively.

window ranging from $E_F - eV/2$ to $E_F + eV/2$ for a given bias voltage V .

In the following, we further clarify the sharp and high minority-spin transmission (T_{\downarrow}) peak of the APC1 state under a bias voltage of +0.4 V. Figure 6(a) shows the distribution of T_{\downarrow} of the APC1 state in the 2DBZ at an energy of 0.17 eV under a bias voltage of +0.4 V. It can be seen from Fig. 6(a) that the high transmissions are mainly distributed near the high-symmetry K point ($k_{\parallel} = 0.33, 0.33$) in the 2DBZ. Correspondingly, the spin-polarized density of states (DOS) at the high-symmetry K point for Fe_3GaTe_2 FME1, the middle Fe_3GaTe_2 FMM layer, and Fe_3GaTe_2 FME2 under a bias voltage of +0.4 V is calculated and shown in Fig. 6(c). It is seen from Fig. 6(c) that the minority-spin DOS of Fe_3GaTe_2 FME1, the majority-spin DOS of Fe_3GaTe_2 FME2, and the minority-spin DOS of the middle Fe_3GaTe_2 FMM layer under a bias voltage of +0.4 V all have a peak at the energy of 0.17 eV, respectively. This corresponds to the occurrence of the resonance tunneling at the K point for the APC1 state of vdW DBMTJ1 under a bias voltage of +0.4 V. To further elucidate the resonance tunneling at the K point for vdW DBMTJ1 under a bias voltage of +0.4 V, the schematic diagrams of the electronic structure of the middle FMM layer and two FMEs at the K point for the APC1 state of vdW DBMTJ1 under a bias voltage of +0.4 V are plotted in Fig. 6(e). It can be seen that the spin states of two FMEs at the K point are discrete energy levels with small widths since our calculations show that the electronic structures of Fe_3GaTe_2 electrodes at the K point exhibit an obvious energy gap and discrete energy levels with small widths around the Fermi energy. As known, a positive bias $+V$ leads the Fermi levels and spin states of FME1 and FME2 to move by $-eV/2$ and $+eV/2$ relative to those of FME1 and FME2 at zero bias, respectively. When

a positive bias of +0.4 V is applied to vdW DBMTJ1, the majority-spin occupied states (E_o) of FME2 are tuned by a bias voltage of +0.4 V to match the minority energy level of the middle FMM layer and the minority-spin unoccupied states (E_u) of FME1, as shown in Fig. 6(e); thus, resonance tunneling occurs at the K point for the APC1 state of vdW DBMTJ1. Consequently, a sharp and high minority-spin transmission peak is produced at an energy of 0.17 eV under a bias voltage of +0.4 V, as shown in Fig. 5(b). Correspondingly, a high minority-spin current is produced for the APC1 state of vdW DBMTJ1 at a positive bias +0.4 V. When the bias voltage is -0.4 V, the peak of the majority-spin DOS of FME1 overlaps with the peak of the minority-spin DOS of FME2 at an energy of 0.17 eV, while it does not overlap with that of the middle FMM layer due to spin splitting of the energy level of the middle Fe_3GaTe_2 FMM layer, as shown in Fig. 6(d). Correspondingly, Fig. 6(f) shows that although the majority-spin occupied states (E_o) of the FME1 are tuned by the bias voltage of -0.4 V to match the minority-spin unoccupied states (E_u) of the FME2, it does not match the majority-spin energy level of the middle FMM layer at a negative bias of -0.4 V. Moreover, it can be seen from Fig. 6(d) that there is also no overlap of the peaks of spin-polarized DOS for FME1, FME2, and the middle FMM layer at other energies within the bias window under a bias voltage of -0.4 V. As a result, there is an absence of the resonance tunneling at the K point for the APC1 state of vdW DBMTJ1 at a bias voltage of -0.4 V, leading to small majority-spin transmission at a bias voltage of -0.4 V, as shown in Fig. 5(b). Therefore, for the APC1 state, the transmission current (minority-spin transmission) of the symmetric vdW DBMTJ1 at positive bias is significantly larger than that at negative bias and thus produces a positive minority-spin conduction and

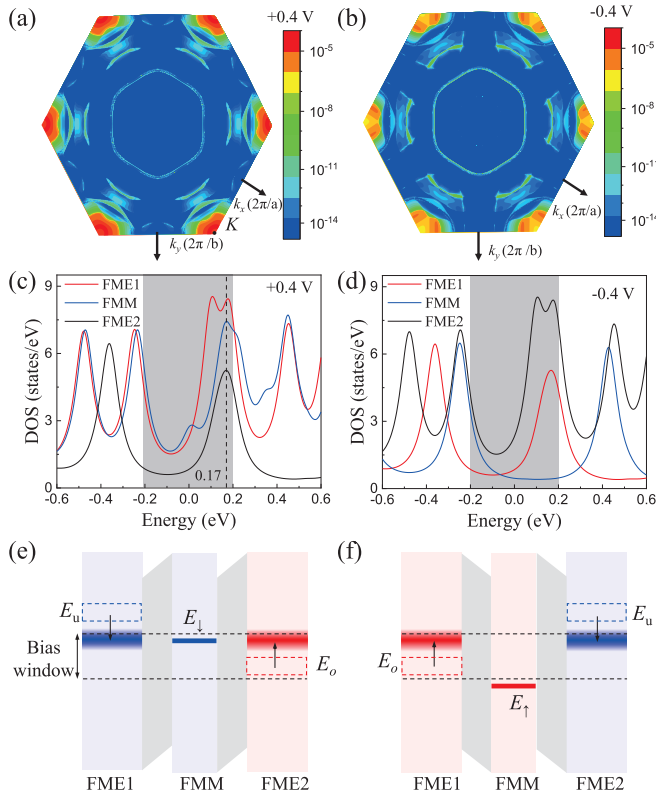


FIG. 6. (a) k -resolved minority-spin transmission (T_{\downarrow}) distributions of vdW DBMTJ1 in the 2DBZ at the energy of 0.17 eV under a bias of +0.4 V. (b) k -resolved majority-spin transmission (T_{\uparrow}) distributions of vdW DBMTJ1 in the 2DBZ at the energy of 0.17 eV under a bias of -0.4 V. The spin-polarized DOS at the high-symmetry K point for the Fe_3GaTe_2 FME1, the middle Fe_3GaTe_2 FMM layer, and the Fe_3GaTe_2 FME2 under the bias voltages of (c) +0.4 V and (d) -0.4 V. Red, blue, and black lines represent the DOS of FME1, FMM, and FME2, respectively. The gray shadows represent the bias window. Schematic diagram of the electronic structure of vdW DBMTJ1 at high-symmetry K point under the bias voltages of (e) +0.4 V and (f) -0.4 V around bias windows. Narrow dotted boxes represent the positions of electronic states of FMEs at zero bias. Thick red and blue lines represent majority-spin and minority-spin states of FMEs and the FMM layer, respectively.

negative cutoff spin diode effect in the symmetric vdW DBMTJ1.

IV. CONCLUSIONS

In conclusion, we propose that when the magnetic moments of the FMEs are antiparallel, a significant spin TD effect can be produced in the symmetric vdW DBMTJ due to the spin splitting of the middle ferromagnetic metal. Taking the symmetric vdW DBMTJ1 and vdW DBMTJ2 as examples to validate the proposed spin TD effect, it is found that three significantly different resistance states can be achieved, which results in giant tunneling magnetoresistances of up to $3.61 \times 10^9\%$ and $1.02 \times 10^6\%$ in vdW DBMTJ1 and vdW

DBMTJ2, respectively. More interestingly, when the magnetic moments of two FMEs are antiparallel, a significant spin TD effect can be produced in vdW DBMTJ1 and vdW DBMTJ2 due to the spin splitting of the middle FM Fe_3GaTe_2 and Fe_3GaTe_2 layers. Moreover, the spin TD effect can be modulated by changing the magnetic configuration of the vdW DBMTJ through a magnetic field. Our calculation results provide good guidance for the development of multifunctional and high-performance microelectronic devices.

ACKNOWLEDGMENTS

This work was financially supported by the National Key Research and Development Program of China (MOST Grant No. 2022YFA1402800), the National Natural Science Foundation of China (NSFC, Grants No. 12134017 and No. 12274175), and the Fundamental Research Funds for the Central Universities. The atomic structures were produced using VESTA software [38]. High-performance computing resources for contributing to the research results were provided by Beijing PARATERA Technology Co., Ltd.

APPENDIX A

As shown in Fig. 7, although the bulk Fe_3GaTe_2 electrode has a metallic electronic structure, the band structure from K to H points exhibits an obvious energy gap around the Fermi energy, and around the Fermi energy, the sum of the states of all k_z points from K to H , are some discrete energy levels with small widths.

APPENDIX B

Figure 8 illustrates the spin-resolved local density of states (LDOS) of vdW DBMTJ1 at the K [$k_{\parallel} = (0.33, 0.33)$] point for the APC1 state under a bias voltage of ± 0.4 V. It can be seen that the LDOS for majority-spin and minority-spin transmission under positive bias voltage differs from that under negative bias voltage. In particular, Fe_3GaTe_2 FME1, Fe_3GaTe_2 FME2, and the middle Fe_3GaTe_2 FMM layer all have states at an energy of 0.17 eV under a bias voltage of +0.4 V, as shown in Fig. 8(b), which corresponds to the

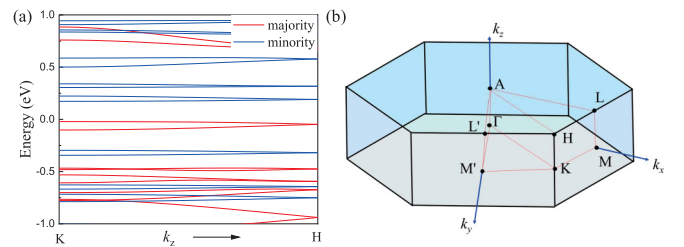


FIG. 7. (a) The band structures of bulk Fe_3GaTe_2 from K to H points in the Brillouin zone. (b) The distribution of k points in the Brillouin zone of bulk Fe_3GaTe_2 .

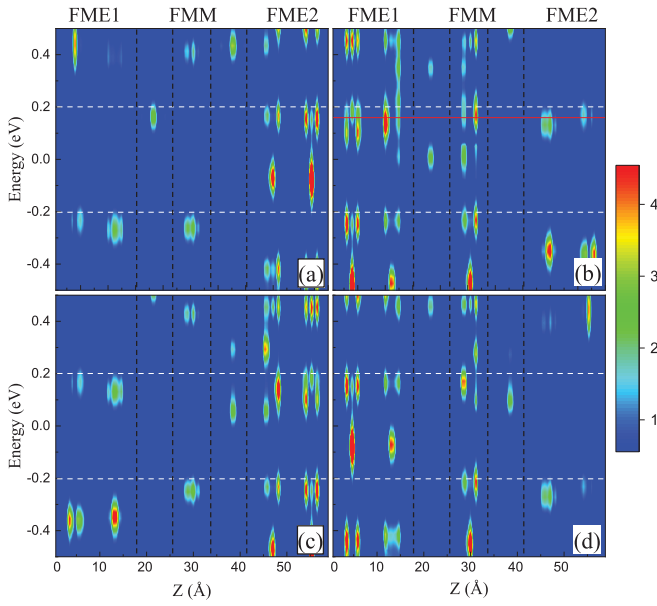


FIG. 8. Spin-resolved LDOS of (a) majority-spin and (b) minority-spin transmission for the APC1 state of vdW DBMTJ1 at $k_{\parallel} = (0.33, 0.33)$ under a bias voltage of $+0.4$ V. Spin-resolved LDOS of (c) majority-spin and (d) minority-spin transmission for the APC1 state of vdW DBMTJ1 at $k_{\parallel} = (0.33, 0.33)$ under a bias voltage of -0.4 V. The red line represents the energy of 0.17 eV.

occurrence of the resonance tunneling at the K point for the APC1 state of vdW DBMTJ1 under a bias voltage of $+0.4$ V.

APPENDIX C

Table II shows the conductance of vdW DBMTJ2 for the APC1, APC2, and PC states under zero bias. The TMR values between the different magnetic states of vdW DBMTJ2 are calculated using formulas (3)–(5). It is notable that the calculated TMR1, TMR2, and TMR3 for vdW DBMTJ2 are as high as $1.02 \times 10^6\%$, $5.77 \times 10^4\%$, and $1.67 \times 10^3\%$, respectively.

APPENDIX D

In order to prove the proposed spin RTD effect in the symmetric vdW DBMTJ, we calculate the I - V curves of vdW DBMTJ2 for the APC1, APC2, and PC states, respectively,

TABLE II. Conductance (e^2/h) of vdW DBMTJ2 for three magnetic configurations under zero bias. G_{total} , G_{\uparrow} , and G_{\downarrow} represent the total, majority-spin, and minority-spin conductances, respectively.

	G_{\uparrow}	G_{\downarrow}	G_{total}
APC1	2.81×10^{-7}	1.92×10^{-9}	2.83×10^{-7}
APC2	5.00×10^{-6}	2.39×10^{-8}	5.02×10^{-6}
PC	2.90×10^{-3}	2.55×10^{-10}	2.90×10^{-3}

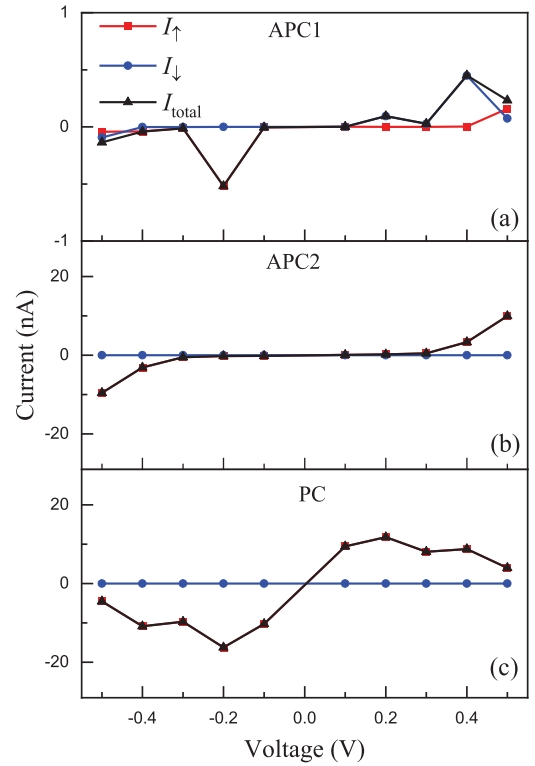


FIG. 9. Spin-resolved current-voltage curve of vdW DBMTJ2 for the (a) APC1, (b) APC2, and (c) PC states. I_{\uparrow} , I_{\downarrow} , and I_{total} ($I_{\uparrow} + I_{\downarrow}$) represent the majority-spin, minority-spin, and total currents, respectively.

As shown in Fig. 9, the majority-spin, minority-spin, and total currents of the APC1 state at positive bias voltages are different from those at corresponding negative bias voltages, while the majority-spin, minority-spin, and total currents at positive bias voltages are almost the same as those at corresponding negative bias voltages in the APC2 and PC states, which means that the reconfigurable spin TD effect also occurs in vdW DBMTJ2.

For vdW DBMTJ2, there is an obvious majority-spin peak at the energy point of 0.096 eV within the bias window under bias voltages of -0.2 V, as shown in Fig. 10(a). This high majority-spin transmission peak within the bias window results in the large current under a bias voltage of -0.2 V. Figure 10(b) shows the distribution of the majority-spin transmission of the APC1 state for vdW DBMTJ2 at the energy of 0.096 eV in the 2DBZ under a bias voltage of -0.2 V. As can be seen, the maximum transmission occurs near the k_1 point [$k_{\parallel} = (0.2, 0.3)$]. Correspondingly, the spin-polarized DOS at the k_1 point $(0.2, 0.3)$ in Fig. 10(c) shows that the high majority-spin transmission peak at the energy of 0.096 eV is attributed to the overlap of the spin-resolved DOS peaks of two Fe_3GaTe_2 FMEs and the middle Fe_3GeTe_2 FMM layer, which is similar to the mechanism by which vdW DBMTJ1 produces the high minority-spin transmission peak at the energy of 0.17 eV under a bias voltage of $+0.4$ V.

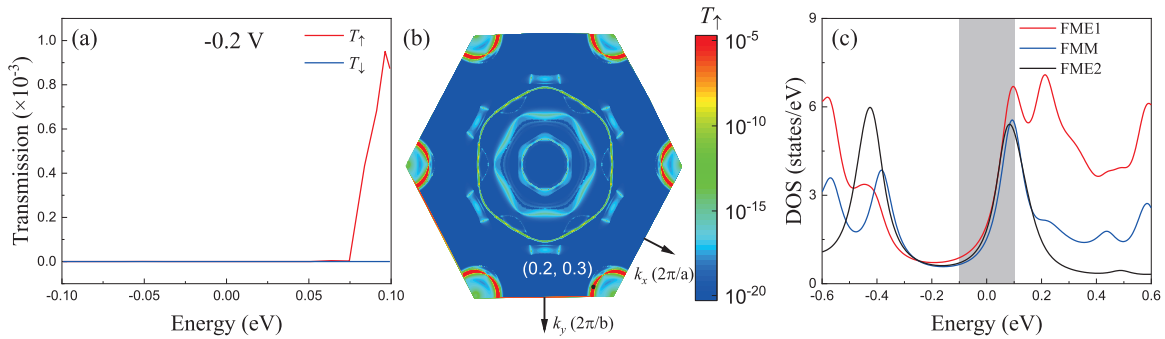


FIG. 10. (a) Spin-resolved transmission spectra of the APC1 state in vdW DBMTJ2 at bias voltages of -0.2 V. The bias window ranges from -0.1 to 0.1 eV. (b) k -resolved majority-spin transmission distributions of vdW DBMTJ2 in the 2DBZ at the energy of 0.096 eV under a bias voltage of -0.2 V. (c) The spin-polarized DOS at the k_{\parallel} point [$k_{\parallel}=(0.2, 0.3)$] for Fe_3GaTe_2 FME1, the middle Fe_3GeTe_2 FMM layer, and Fe_3GaTe_2 FME2 under a bias voltage of -0.2 V. The gray shadow represents the bias window.

- [1] F. Sun, J. Chen, X. Lin, and D. Liao, Analysis and suppression of rectifier diode voltage oscillation mechanism in IPOS high-power PSFB converters, *Electronics* **12**, 2871 (2023).
- [2] Z. He, J. Lan, and C. Liu, Compact rectifiers with ultra-wide input power range based on nonlinear impedance characteristics of Schottky diodes, *IEEE Trans. Power Electron.* **36**, 7407 (2021).
- [3] H. K. O'Brien, W. Shaheen, A. Ogunniyi, C. Scozzie, L. Cheng, M. Hinojosa, K. Lawson, S. Lacouture, and S. Bayne, Large chip area SiC PiN diodes demonstrated for thyristor protection in a pulsed system, in *2014 IEEE International Power Modulator and High Voltage Conference (IPMHVC)* (IEEE, New York, 2014).
- [4] C.-Y. Lin, P.-H. Wu, and M.-D. Ker, Area-efficient and low-leakage diode string for on-chip ESD protection, *IEEE Trans. Electron Devices* **63**, 531 (2016).
- [5] Y. Ding, X. Xu, A. Bhalla, X. Yang, J. Chen, and C. Chen, Switchable diode effect in BaZrO_3 thin films, *RSC Adv.* **6**, 60074 (2016).
- [6] S. Liu, D. S. Shah, and R. Kramer-Bottiglio, Highly stretchable multilayer electronic circuits using biphasic gallium-indium, *Nat. Mater.* **20**, 851 (2021).
- [7] X. Jin, X. Yuan, S. Zhang, M. Li, and X. Liu, Complementary doped source-based reconfigurable Schottky diode as an equivalence logic gate, *ACS Omega* **8**, 23120 (2023).
- [8] L. Esaki, New phenomenon in narrow germanium $p-n$ junctions, *Phys. Rev.* **109**, 603 (1958).
- [9] Y. Zhang, M. Sun, D. Piedra, M. Azize, X. Zhang, T. Fujishima, and T. Palacios, GaN-on-Si vertical Schottky and $p-n$ diodes, *IEEE Electron Device Lett.* **35**, 618 (2014).
- [10] E. Şaşıoğlu and I. Mertig, Theoretical prediction of semiconductor-free negative differential resistance tunnel diodes with high peak-to-valley current ratios based on two-dimensional cold metals, *ACS Appl. Nano Mater.* **6**, 3758 (2023).
- [11] Z. Zhang, B. Zhang, Y. Wang, M. Wang, Y. Zhang, H. Li, J. Zhang, and A. Song, Toward high-peak-to-valley-ratio graphene resonant tunneling diodes, *Nano Lett.* **23**, 8132 (2023).
- [12] H. Yuan, R. Xu, J. Ren, J. Yang, S. Wang, D. Tian, Y. Fu, Q. Li, X. Peng, and X. Wang, Anisotropic charge transfer and gate tuning for $p\text{-SnS}/n\text{-MoS}_2$ vertical van der Waals diodes, *Nanoscale* **15**, 15344 (2023).
- [13] B. Radisavljevic, A. Radenovic, J. Brivio, V. Giacometti, and A. Kis, Single-layer MoS_2 transistors, *Nat. Nanotechnol.* **6**, 147 (2011).
- [14] W. Wu, L. Wang, Y. Li, F. Zhang, L. Lin, S. Niu, D. Chenet, X. Zhang, Y. Hao, T. F. Heinz, J. Hone, and Z. L. Wang, Piezoelectricity of single-atomic-layer MoS_2 for energy conversion and piezotronics, *Nature (London)* **514**, 470 (2014).
- [15] X. Cai, T. Song, N. P. Wilson, G. Clark, M. He, X. Zhang, T. Taniguchi, K. Watanabe, W. Yao, D. Xiao, M. A. McGuire, D. H. Cobden, and X. Xu, Atomically thin CrCl_3 : An in-plane layered antiferromagnetic insulator, *Nano Lett.* **19**, 3993 (2019).
- [16] A. M. Afzal, Y. Javed, N. A. Shad, M. Z. Iqbal, G. Dastgeer, M. M. Sajid, and S. Mumtaz, Tunneling-based rectification and photoresponsivity in black phosphorus/hexagonal boron nitride/rhenium diselenide van der Waals heterojunction diode, *Nanoscale* **12**, 3455 (2020).
- [17] E. Şaşıoğlu, T. Aull, D. Kutschabsky, S. Blugel, and I. Mertig, Half-metal-spin-gapless-semiconductor junctions as a route to the ideal diode, *Phys. Rev. Appl.* **14**, 014082 (2020).
- [18] E. Şaşıoğlu, S. Blugel, and I. Mertig, Proposal for reconfigurable magnetic tunnel diode and transistor, *ACS Appl. Electron. Mater.* **1**, 1552 (2019).
- [19] S. Yu, W. Shi, Q. Li, F. Xu, L. Gu, and X. Wang, Reconfigurable spin tunnel diodes by doping engineering VS_2 monolayers, *Phys. Chem. Chem. Phys.* **25**, 26211 (2023).
- [20] K. Murali, M. Dandu, S. Das, and K. Majumdar, Gate-tunable $\text{WSe}_2/\text{SnSe}_2$ backward diode with ultrahigh-reverse rectification ratio, *ACS Appl. Mater. Interfaces* **10**, 5657 (2018).
- [21] X. Liu, D. Qu, H.-M. Li, I. Moon, F. Ahmed, C. Kim, M. Lee, Y. Choi, J. H. Cho, J. C. Hone, and W. J. Yoo, Modulation of quantum tunneling via a vertical two-dimensional black phosphorus and molybdenum disulfide $p-n$ junction, *ACS Nano* **11**, 9143 (2017).
- [22] X. Han, L. Tao, H. Wu, P. Tang, and Y. Xing, Electron and magnon resonant tunneling: Materials, physics and devices, *J. Phys. D: Appl. Phys.* **56**, 443001 (2023).

- [23] G. Kresse and J. Hafner, *Ab initio* molecular dynamics for liquid metals, *Phys. Rev. B* **47**, 558 (1993).
- [24] G. Kresse and J. Furthmüller, Efficient iterative schemes for *ab initio* total-energy calculations using a plane-wave basis set, *Phys. Rev. B* **54**, 11169 (1996).
- [25] D. M. Ceperley and B. J. Alder, Ground state of the electron gas by a stochastic method, *Phys. Rev. Lett.* **45**, 566 (1980).
- [26] J. P. Perdew and A. Zunger, Self-interaction correction to density-functional approximations for many-electron systems, *Phys. Rev. B* **23**, 5048 (1981).
- [27] J. P. Perdew, K. Burke, and M. Ernzerhof, Generalized gradient approximation made simple, *Phys. Rev. Lett.* **77**, 3865 (1996).
- [28] X. Li, M. Zhu, Y. Wang, F. Zheng, J. Dong, Y. Zhou, L. You, and J. Zhang, Tremendous tunneling magnetoresistance effects based on van der Waals room-temperature ferromagnet Fe_3GaTe_2 with highly spin-polarized Fermi surfaces, *Appl. Phys. Lett.* **122**, 082404 (2023).
- [29] S. Grimme, J. Antony, S. Ehrlich, and H. Krieg, A consistent and accurate *ab initio* parametrization of density functional dispersion correction (DFT-D) for the 94 elements H-Pu, *J. Chem. Phys.* **132**, 154104 (2010).
- [30] J. Taylor, H. Guo, and J. Wang, *Ab initio* modeling of quantum transport properties of molecular electronic devices, *Phys. Rev. B* **63**, 245407 (2001).
- [31] J. Taylor, H. Guo, and J. Wang, *Ab initio* modeling of open systems: Charge transfer, electron conduction, and molecular switching of a C_{60} device, *Phys. Rev. B* **63**, 121104(R) (2001).
- [32] Y. Deng, Y. Yu, Y. Song, J. Zhang, N. Z. Wang, Z. Sun, Y. Yi, Y. Z. Wu, S. Wu, J. Zhu, J. Wang, X. H. Chen, and Y. Zhang, Gate-tunable room-temperature ferromagnetism in two-dimensional Fe_3GeTe_2 , *Nature (London)* **563**, 94 (2018).
- [33] Z. Fei, B. Huang, P. Malinowski, W. Wang, T. Song, J. Sanchez, W. Yao, D. Xiao, X. Zhu, A. F. May, W. Wu, D. H. Cobden, J.-H. Chu, and X. Xu, Two-dimensional itinerant ferromagnetism in atomically thin Fe_3GeTe_2 , *Nat. Mater.* **17**, 778 (2018).
- [34] G. Zhang, F. Guo, H. Wu, X. Wen, L. Yang, W. Jin, W. Zhang, and H. Chang, Above-room-temperature strong intrinsic ferromagnetism in 2D van der Waals Fe_3GaTe_2 with large perpendicular magnetic anisotropy, *Nat. Commun.* **13**, 5067 (2022).
- [35] D.-F. Shao, J. Ding, G. Gurung, S.-H. Zhang, and E. Y. Tsymbal, Interfacial crystal Hall effect reversible by ferroelectric polarization, *Phys. Rev. Appl.* **15**, 024057 (2021).
- [36] A. Marjaoui, M. A. Tamer, M. Diani, A. El Kasmi, and M. Zanouni, First-principles investigations of structural, electronic and thermoelectric properties of $\beta\text{-Sb/GeI}_2$ van der Waals heterostructures, *J. Comput. Electron.* **21**, 582 (2022).
- [37] K. Yakushiji, K. Noma, T. Saruya, H. Kubota, A. Fukushima, T. Nagahama, S. Yuasa, and K. Ando, High magnetoresistance ratio and low resistance-area product in magnetic tunnel junctions with perpendicularly magnetized electrodes, *Appl. Phys. Express* **3**, 053003 (2010).
- [38] K. Momma and F. Izumi, *VESTA 3* for three-dimensional visualization of crystal, volumetric and morphology data, *J. Appl. Crystallogr* **44**, 1272 (2011).